On the structural, mechanical, and biodegradation properties of HA/β-TCP robocast scaffolds

Manuel Houmard, Qiang Fu, Martin Genet, Eduardo Saiz, Antoni P. Tomsia

On the Structural, Mechanical and Biodegradation Properties of HA/β-TCP Robocast Scaffolds

Manuel Houmard[a], Qiang Fu[a], Martin Genet[a], Eduardo Saiz[b], Antoni P. Tomsia[a]

[a] Materials Science Division, Lawrence Berkeley National Laboratory, Berkeley, CA 94720, USA

[b] Centre for Advanced Structural Ceramics, Department of Materials, Imperial College London, UK

Abstract: Hydroxyapatite/β-tricalcium phosphate, HA/β-TCP, composite scaffolds have shown great potential for bone-tissue engineering applications. In this work, ceramic scaffolds with different HA/β-TCP compositions, pure HA, 60HA/40β-TCP and 20HA/80β-TCP, were fabricated by a robotic-assisted deposition (robocasting) technique using water-based hydrogel inks. A systematic study was conducted to investigate the porosity, mechanical property and degradation of the scaffolds. Our results indicate that, at a similar volume porosity, the mechanical strength of the sintered scaffolds increased with the decreasing rod diameter. The compressive strength of the fabricated scaffolds (porosity = 25 – 80 vol%) varied between ~3 to ~50 MPa, a value equal or higher than that of human cancellous bone (2 – 12 MPa). Although there was a slight increase of Ca and P ions in water after 5 month, no noticeable degradation of the scaffolds in SBF or water was observed. Our findings from this work indicate that composite calcium phosphate scaffolds with customer-designed chemistry and architecture may be fabricated by a robotic-assisted deposition method.

Keywords: Calcium Phosphates, HA/β-TCP composites, Robocasting, Biomedical Scaffolds, Tissue Engineering

---

1. Introduction

Calcium phosphate (CaP) ceramics, especially biphasic calcium phosphate (BCP) composed of hydroxyapatite (HA, $Ca_{10}(PO_4)_6(OH)_2$) and β-tricalcium phosphate (β-TCP, $Ca_3(PO_4)_2$), are widely used as bone-substitute material and in various tissue-engineering applications [1-8]. Indeed, there is a growing

interest in BCP because it has been shown that this material improves the formation of new bone inside the implanted scaffold [3,4]. The literature indicates that the faster dissolution rate of β-TCP would be greatly responsible of this enhancement. However, in vitro tests indicate that fast dissolution can decrease the mechanical strength of CaP scaffolds [9]. Furthermore, studies reported that HA has higher mechanical strength and lower degradation rate than β-TCP [4,10,11]. Therefore, the HA/β-TCP ratio is a key parameter controlling the performance of the scaffold for bone repair applications, since it determines both degradation rate and mechanical properties of the material [12]. Scaffolds for bone regeneration require interconnected macro- (> 50 μm) and micro-pores (1 – 50 μm) that create favorable conditions for cell seeding, proliferation and vascularization, and new bone formation [13]. An optimal three-dimensional (3-D) scaffold must be strong enough to replace the bone, at least temporarily, while providing a substrate for cell attachment and proliferation. It also must dissolve gradually as new tissue grows [14]. To fulfill the above mentioned criteria, new processing routes with the ability to produce BCP scaffolds with controlled and organized micro- and macro-pores are needed for scaffold fabrication.

A variety of techniques has been used to fabricate porous ceramic scaffolds for tissue engineering, including replica templates [15,16], emulsions [17], the use of porogens [18], freeze-casting [19], and solid freeform fabrication (robocasting) [9,15,20-23]. Among them, the solid freeform fabrication system probably offers the best control of the macro-porosity and facilitates the complex shape formation required for bone scaffolds [9,15,20-23]. The robocasting method used in this study is a printing process that builds 3-D structures layer-by-layer by extruding a continuous filament, or rod, through a tip guided by a computer-assisted positioning system [9,15,20-23]. The technique permits printing with outstanding spatial resolution and has been used to print ceramic grids with line and width diameters varying from hundreds of microns to sub-micron levels [23]. The technique also allows easy modification of the chemistry by adjusting the ink composition and the optimization of the architecture for enhanced mechanical properties of the scaffolds. The aim of the present work was to investigate the structure-property relationship of calcium phosphate scaffolds prepared by a robocasting technique. A systematic study was carried out on the porosity, mechanical property and degradation of scaffolds with three different compositions, pure HA, 60HA/40β-TCP and 20HA/80β-TCP.

2. Experimental

2.1. Ink preparation

Ceramic inks were prepared by mixing ceramic powders with a Pluronic F-127 solution according to a previous work [20]. The Pluronic solution exhibits a reverse thermal behavior: it is fluid at low temperatures (close to 0ºC) but a soft gel at room temperature. This reverse behavior makes easy the dispersion of the HA/β-TCP ceramic powders into the Pluronic solution at low temperature and forms a gel enough viscous to print scaffolds at room temperature. The solution was prepared by mixing a Pluronic powder with deionized water (20 wt% of Pluronic) for 5 h using zirconia balls in a shaker (Red Devil 5400, Red Devil Equipment Co., Plymouth, MN). Next, the solution was cooled to ~0ºC in a water/ice bath and then, the ceramic powders were added while maintaining the solution at low temperature to ensure the complete reverse gellation process and to lower the viscosity. In order to ensure homogeneity, the inks were mixed thoroughly for 10 min in the water/ice bath and afterwards sieved through a 75 μm mesh to minimize the presence of aggregates. The inks were loaded into 10 mL syringes (BD, Franklin Lakes, NJ) with an HD-PTFE custom sized plunger. The syringes were gently tapped from the bottom to move remaining bubbles to the top. Three ceramic powders with different compositions, HA, 60HA/40β-TCP and 20HA/80β-TCP (Trans-Tech, Adamstown, MD) were used for the ink preparation. The average particle size and the specific surface area of the powders are summarized in Table 1 and the formulations of the inks are listed in Table 2.

2.2. Scaffold printing

HA/β-TCP ceramic cube grids (~ 7 x 7 x 7 mm^3 before sintering) were fabricated using a robotic deposition device (Robocad 3.0, 3-D Inks, Stillwater, OK) [9,15,20-22]. The diameter of the ceramic rods, 200-610 μm, was controlled by the size of the printing tips (EFD precision tips, EFD, East Providence, RI). The distance between the printed rods was varied from 100 to 620 μm and the layer height, which depends of the rod diameter, was fixed at ~75% of the tip diameter to form a strong bonding between the successive layers. The scaffolds were printed inside a reservoir of non-wetting oil (Lamplight, Menomonee Falls, WI) over a mirror-polished silicon wafer (0.6 mm thick). Since the silicon surface is hydrophilic, it presents a certain degree of adhesion with the first printed line so that the scaffold remains stable during printing. The smooth and inert mirror-polished surface allows easy removal of the samples after fabrication which facilitates handling and prevents deformations due to uneven shrinkage during drying and sintering. After printing, the samples were dried for two days at room temperature, removed from the substrate, and sintered on top of zirconia balls (500 μm diameter) to favor a homogeneous shrinkage. Scaffolds were fired at 600ºC (2ºC/min heating rate)

for 2 hours to burnout the organics, followed by sintering for 2 h at 1275°C for HA and at 1100°C for composite samples with a heating and cooling rate of 5°C/min. The temperature of 1100°C for the composite structures was chosen to avoid the formation of α-TCP crystals during sintering as they can generate micro-cracks due to volume changes thus decreasing the mechanical performance of the scaffolds [20,24].

2.3. Characterization

X-Ray Diffraction (XRD) (Siemens D-500, Munich, Germany, Cu Kα1 = 1.5406 Å) was used to identify the phases present in the sintered scaffolds. The acquisitions were carried out at a scanning rate of 1.8 °/min in the 2θ range of 20–80° after grinding the scaffolds to powder. The spectra were compared with HA and β-TCP JCPDS cards 09-0432 and 09-0169 respectively. As a result, matching the peak intensities of each phase, the percentage of HA and β-TCP phases in the powders and scaffolds were approximated. The α-TCP phase is identified using JCPDS card 09-0348.

Morphology of the scaffolds was examined with scanning electron microscopy (SEM) (Hitachi FE-SEM-4300EN). The scaffolds were sputter-coated with gold and examined at an accelerating voltage of 10 kV.

The density of the scaffolds was calculated from the mass and dimensions of at least five samples with regular shapes. The theoretical densities of HA (3.16 g/cm^3) and β-TCP (3.14 g/cm^3) were then used as references to calculate the total volume fraction of porosity. The open porosity was measured using the Archimedes' method employing kerosene as the liquid.

The compressive strength of the scaffolds was measured on a servo-hydraulic testing machine (MTS810, MTS Systems, Eden Prairie, MN) with a crosshead speed of 0.2 mm/min, for at least five samples from the same batch.

Synchrotron X-ray micro computerized tomography was used to obtain a 3-D perspective of the scaffold. Scanning was conducted at the Beamline 8.3.2, Advanced Light Source (ALS-LBNL, Berkeley, CA) with 22 keV monochromatic X-rays and a 4.4 μm voxel size (resolution). The data sets were reconstructed using Octopus software and the three-dimensional visualization was performed using Avizo software.

Degradation of scaffolds was evaluated by determining the scaffold weight loss as a function of the immersion time in simulated body fluid (SBF) with a starting pH of ~7.2 at 37°C. The composition of the SBF corresponds to the corrected SBF solution previously published by Kokubo [25]. A ratio of 1 g of scaffold to 100 mL of SBF was used for each test. After removal from the SBF at selected times, the scaffolds were dried at 100°C and weighed. The weight loss was defined as $\Delta W_t = (W_0 - W_t) / W_0$, where W_0 is the initial mass of the scaffolds and W_t is the mass at time t. The solution was cooled from 37°C to room temperature, and its pH measured using a pH meter. Weight loss of the scaffolds in deionized water was also evaluated with a ratio of 1 g of scaffold to 20 mL of water.

Ca and P concentrations in the SBF and water solutions, after immersion of the scaffolds for 1 and 5 months respectively, were analyzed using ICP (Inductively Coupled Plasma atomic emission spectrometer, Perkin Elmer Optima 3000).

3. Results and discussion

3.1. General aspects

3.1.1. Printing of scaffolds

Three-dimensional scaffolds were printed by extruding inks through cone tips from 200 to 610 µm. Sintered scaffolds (printed with a 250 µm cone tip) are illustrated in Figure 1. This figure shows a entire view of the sintered scaffolds (Figure 1A) and detailed morphologies (Figure 1B – F). Three-dimensional reconstructions of a scaffold and a rod intersection using synchrotron X-ray micro-computed tomography are also illustrated (Figures 1G and 1H, respectively). These images demonstrate the excellent capability of the technique in the production of periodical scaffolds with an accurate controlled and interconnected macro-porosity. The macro-pore size in the x and y directions (i.e., parallel to the sample support, see Figure 1B) is determined by the program settings in the printing process (see Section 2.2). For target values ranging from 100 to 620 µm before sintering, values ranging from 80 to 550 µm were observed after sintering. The macro-pore size in the z direction (i.e., perpendicular to the sample support, see Figure 1B) is directly linked to the rod diameter (see Section 2.2). Thus, for as-printed scaffolds with rod diameters ranging from 200 to 610 µm before sintering, pores ranging from 60 to 250 µm were observed in sintered samples. Such pore dimensions may promote cell seeding, proliferation and vascularization, and bone formation inside the scaffold as literature

indicates that pores in the range of 100 – 400 μm are optimal for the bone ingrowth [26-30]. This macro-porosity must also provide transport pathways for nutrients, oxygen, and wastes necessary to maintain living cells within the scaffold. The images (Figure 1D-F) also show a slight deformation of the rods that was caused by the gravity during the printing, drying and sintering steps. This deformation effect was more readily seen in scaffolds printed with larger tip (620 μm in Figure 1E) than smaller one (330 μm in Figure 1F). Nevertheless, the adhesion between the rods is strong (Figure 1H), which implies a reasonable mechanical strength for tissue engineering applications.

3.1.2. Composition

Crystalline phases in the sintered scaffolds were detected by XRD. Figure 2 shows XRD spectra of the HA and composite scaffolds sintered at 1275ºC and 1100ºC, respectively. A small amount of α-TCP phase (Figure 2a) was present in the spectrum of HA scaffold, which was resulting from the impurities in the as-received powder (see Table 1). Only HA and β-TCP phases were observed in the sintered composite scaffolds (Figures 2b and 2c). HA/β-TCP scaffolds ratio in the composite scaffolds was determined by matching the peak intensities with the JCPDS patterns. Ratios of 59/41 and 16/84 for the spectra of 60HA/40β-TCP and 20HA/80β-TCP scaffolds were obtained, respectively. These values are close to those provided by the powder manufacturer, an indication that the robocasting and sintering processes does not significantly affect the chemistry of the materials. In order to justify the sintering treatment at 1100°C for the composite scaffolds, a XRD acquisition for a 20HA/80β-TCP scaffold sintered at 1140ºC is also illustrated in Figure 2. This spectrum not only shows the presence of HA and β-TCP phases, but also the presence of α-TCP phase was detected. This example indicates that α-TCP crystals can be generated in both 60HA/40β-TCP and 20HA/80β-TCP composite scaffolds during the sintering treatment at 1140°C. Moreover, as mentioned previously, the presence of α-TCP phase can induce micro-cracks in the scaffold structure that would decrease its mechanical strength. Thus, the 60HA/40β-TCP and 20HA/80β-TCP composite scaffolds in this work were sintered at 1100ºC to avoid the generation of micro-cracks in their structure.

3.1.3. Shrinkage

The shrinkage of the scaffolds after sintering was systematically studied as a function of the width between the rods for the three compositions for scaffolds printed with tip diameter of 250 μm. Figure 3 shows the scaffold shrinkage in the three directions x, y and z, for the three compositions as a function of the as-printed macro-pore size. First, the shrinkage does not depend on the width between the rods and it is about the

same in all directions. Only a slight increase in the shrinkage is observed in the z direction, which was due to a slight effect of the gravity during the drying and sintering steps. Shrinkages of ~16 %, ~8 % and ~14 % were measured for HA (Figure 3a), 60HA/40β-TCP (Figure 3b) and 20HA/80β-TCP (Figure 3c) scaffolds, respectively. The shrinkages values measured for HA and 20HA/80β-TCP scaffolds seem to indicate the choice of efficient sintering conditions for these compositions. The lower shrinkage ratio for the 60HA/40β-TCP scaffolds could result from a sintering temperature (1100°C) too far away from the adequate sintering temperature of the HA phase, which is the major component of this composition. However, according to the previous section, the sintering temperature of the 60HA/40β-TCP scaffolds cannot be increased due to the possible formation of undesirable α-TCP crystals in the structure at higher temperatures. To conclude, the shrinkages are higher for HA and rich β-TCP scaffolds since the sintering temperatures are better adjusted for these compositions.

3.2. Total and open porosities

Porosity of HA, 60HA/40β-TCP and 20HA/80β-TCP scaffolds was controlled by varying the width between the rods in the x-y plan during the printing process (macro-pores from 100 to 620 µm). Total and open porosities of the scaffolds were measured as a function of the width between the rods for the three types of scaffolds printed with tip diameter of 250 µm. Figure 4 presents the open and total porosities of the scaffolds as a function of the macro-pore size before sintering. The figure shows that with the increase of the width between the rods, i.e., the macro-pore size, both open and total volume porosities increase regardless of the composition of the scaffold. The close value between the total and open porosities indicates that the majority of the pores in the printed structures are open. HA scaffolds exhibit higher amount of closed pores than the composite scaffolds, as will be discussed later. Also, HA scaffolds exhibit the lowest open and total porosities, and the difference with the composite structures became more obvious for smaller macro-pore sizes. Figure 4 also shows that, when printed with the same micro-pore size, 60HA/40β-TCP scaffolds are slightly more porous than 20HA/80β-TCP counterparts. The total porosity measured here includes both the macro-pores defined by the rod spacing designed during printing and the micro-pores present inside the rods. This micro-porosity results from both sintering conditions and burnout of the organics present in the initial inks, including Pluronic and water. In order to compare porosity variations between the three compositions, rod's micro-porosity were observed by SEM.

Figure 5 shows pictures of the surface and fracture of the rods in HA, 60HA/40β-TCP and 20HA/80β-TCP scaffolds. The HA rods show the densest structure (Figures 1D and 5A-D) resulting from the highest shrinkage ratio (Figure 3) and the highest amount of ceramic matter in the initial ink (Table 2). In contrast, composite rods show a higher amount of micro-pores with two different range sizes: one of ~20-30 μm (Figures 1E and 1F) and a smaller one of ~1 μm (Figures 5B-C and 5E-F). However, the rods from 60HA/40β-TCP and 20HA/80β-TCP scaffolds do not show identical morphologies. The 20HA/80β-TCP rods present a porous structure with relatively well sintered grains, in agreement with the shrinkage data, while the 60HA/40β-TCP exhibit separated particles among interconnected and smaller micro-pores (Figure 5). The 20HA/80β-TCP micro-pores are larger than those of the 60HA/40β-TCP structure probably due to the higher amount of organics in the initial paste. These SEM observations correspond well with the data in Figure 4. Indeed, composite rods are full of micro-pores leading to an almost completely open porosity, while the HA rods are much denser yielding a higher amount of closed pores (Figure 4). Also, since HA rods are much denser than the composite ones, the porosity decreases even faster with increasing number of rods (Figure 4). Finally, even if the pore morphologies differ, the total and open porosity values in both composite are quite similar which must result from variations in the sintering process and ink compositions. Indeed, the sintering is less efficient for the 60HA/40β-TCP composition, but on the other hand its initial amount of ceramic is higher. Porosity will have an influence on the mechanical performance of the bone scaffolds. To conclude, the important presence of micro-porosity in BCP rods, which is not observed in HA, could be a key to explain enhanced bone ingrowth performance of such materials reported in the literature.

.

3.3 Mechanical strength

3.3.1. Effect of the diameter of the rod

As described earlier, scaffolds were printed with cone tips ranging from 200 to 610 μm in diameter. The effect of the rod size on the mechanical properties of HA scaffolds was investigated. Constant porosity (45 vol%) was achieved by adjusting the width between the printed rods to accommodate the differences in their rod diameters. Figure 6 shows compressive strength of HA scaffolds as a function of the tip diameter. When the tip diameter increases from 200 to 610 μm, significant decrease of the mechanical properties occurs, from 23 to 8 MPa. To understand this observation, typical stress - deformation curves are illustrated in insets of the Figure 6 for scaffolds printed with tip diameters of 250 and 510 μm (insets A and B, respectively). First, as observed in a previous work [22], these insets show that the rupture mechanism of the robocast structures is

not as sudden as a bulk ceramic. Indeed, the stress does not increase linearly until final rupture; it goes up and down due to the numerous cracks appearing in the scaffold during the deformation, which damage the structure and decrease its stiffness. Then, for scaffold printed with a smaller tip, the number of rods is higher (at a constant porosity) and the successive cracks present in the scaffold are not catastrophic since the remaining rods are strong enough to bear the stress along the applied deformation (inset A of figure 6). The stars included in the inset illustrate some obvious cracks occurring in the structure during the compressive test. When the stress become too high for the structure, the sample collapses completely resulting in a sudden decrease of the stress (inset A of figure 6). In contrast, for scaffolds printed with a larger tip, the inset B of Figure 6 shows that the successive cracks (some cracks are indicated by a star) seem to induce significant defects and the structure could not withstand high stresses during the deformation. To conclude, these results point out the interest in fabricating very thin structures to get stronger porous materials for various applications.

3.3.2 Effect of the macro-pore size

The compressive strength of the scaffolds as a function of their total porosity is shown in Figure 7 for scaffolds printed with a tip diameter of 250 µm. The figure indicates that the compressive strength gradually increases, as expected, when the total porosity decreases for all three compositions. Then, few differences in the compressive strength are observed between the compositions for a given porosity. The 20HA/80β-TCP scaffolds is slightly stronger than the other two when the porosity decreases below 60 vol%. This behavior probably results from a relatively better sintering than 60HA/40β-TCP, which give strength to the structure, even if there is still an important micro-porosity in the rods (see Figures 5C-F). Mechanical tests performed on 60HA/40β-TCP indicate lower strength in the x and y directions parallel to the printing plan (inset of the figure 7). However, the values are very close to each other in agreement with early claims indicating that robocasted grid scaffolds exhibit quite similar compressive strength in all directions [21]. Figure 7 also shows that regardless of the composition the compressive strengths of the fabricated scaffolds (in all three directions) were higher or in the same range as those reported for human cancellous bone (2 – 12 MPa). According to a recent review on CaP scaffolds [31], the measured compressive strengths are similar to those reported in the literature for HA/β-TCP scaffolds with similar porosity [32,33]. Moreover, since the macro-pore size is an important factor for bone ingrowth into scaffold [26-30], Figure 8 shows the scaffold compressive strength as a function of the macro-pore size for the three compositions. Figure 8 indicates that for a given macro-pore size, the strength of the scaffolds varies in the order HA > 20HA/80β-TCP > 60HA/40β-TCP. This

classification results from variation in rod structures and especially the presence of micro-pores. This corresponds well with the observation from Figure 5 which shows a better sintering of the HA particles yielding to very dense rods and thus stronger scaffolds. Then, the micro-porous 20HA/80β-TCP structure presented well sintered grains compared with the 60HA/40β-TCP one (Figure 5), which explains the difference between the strength of composite samples. In other words, for a same macro-pore size, the strength of the scaffold is controlled by the micro-porosity and the sintering efficiency. To conclude, the compressive strengths measured here are high enough for scaffold handling which makes these materials good candidate for *in vitro* or *in vivo* experiments. And for specified applications requiring certain strength and minimal macro-pore size, Figure 8 allows us to choose the possible scaffold compositions to fill the corresponding bone defect.

3.4. Design of the scaffold

Figure 9 shows some examples of patterns designed by robocasting with the HA/β-TCP composition studied here. Scaffolds with a gradient porosity in the x-y directions were fabricated (Figures 9A-B). Figure 9C illustrates the production of bio-inspired scaffold with a radial gradient: highly porous in the middle and denser at the external perimeter, mimicking the structure of a real bone. Also, alternated pattern and gradient in the z axis can be obtained as presented in Figures 9D and 9E, respectively. These patterns indicate the capability of the device which allows excellent control of the ceramic design and spatial distribution of porosity. All these characteristics could play important roles in the scaffold performance. Since the porosity must provide transport pathways for nutrients, oxygen, and wastes necessary to maintain the cells alive inside the scaffold, its design has certainly a preponderant influence on the *in vitro* and *in vivo* performance. Modifying the structure of the scaffold could also affect its mechanical properties. That is why numerical models are currently being developed in our research group to predict the mechanical properties of such robocast ceramics [34]. These studies would be able to provide directions to improve the mechanical properties of the scaffold as a function of its design, although, compromises between enhanced mechanical properties and improved bone ingrowth may have to be made.

3.5. In vitro degradation

The great interest of HA/β-TCP composite scaffolds for bone regeneration is based on the preferential dissolution of the β-TCP phase [3,4]. Thus, adjusting the HA/β-TCP ratio should lead to a control of the scaffold degradation and its replacement by new bone. In this context, the degradation of the robocast scaffold in SBF was studied as a function of the HA/β-TCP composition during a static immersion for one month. Figures 10 and 11 show pH and scaffold weight changes as a function of the immersion time for the three compositions studied. Figure 10 exhibits gradual increase of the pH value of SBF during the immersion. The value reached ~7.55 for all three compositions. The SBF solution containing the 20HA/80β-TCP samples appears to have the fastest dissolution rate while the one with the 60HA/40β-TCP composites the slowest one. In agreement with the literature, changes in pH during SBF immersion could be attributed to the dissolution of CaP releasing Ca^{2+}, PO_4^{3-} and OH^- ions in solution, which then would precipitate as carbonate apatite on the material surface [35-37]. The release of Ca^{2+} and OH^- ions led to an increase in the pH value of SBF. Moreover, variation in pH for the different compositions could result from differences in HA/β-TCP ratio, grain size, and porosity of the scaffolds [36,38]. Figure 11 shows the weight loss of the scaffolds after immersion in SBF for one month. No significant weight loss was observed for all scaffolds (< 1%). The results is contradicting to the literature reports, which claim BCP scaffolds degrades much faster than HA [3,4]. However, to the authors' knowledge, there is no direct measurement of the weight loss of such BCP scaffold in vitro or in vivo. The weight loss data correspond well with Ca and P concentration in SBF measured by ICP (Table 3). The data show that Ca and P concentration after immersion of HA samples during one month almost did not change the solution composition. For the solutions where composite scaffolds where immersed, there was decrease in the concentration of Ca and P. However, the decrease was very small (~1.0 mMol/L for Ca and P, respectively) and did not account for the formation of any crystals on the scaffold surface. These results indicate that the degradation of such ceramic structures in static SBF solution was very slow. Dynamic system and/or longer immersion time may be more appropriate to observe a significant degradation of such scaffolds.

In order to investigate the degradation of these scaffolds, another experiment was conducted by immersion in water. Although water is different from SBF or human blood plasma, this testing gives a better understanding and direct measurement of the degradation rate. Weight loss and ICP measurements are reported in Figure 12 and Table 3, respectively. Figure 12 does not present any variation of mass for the three compositions studied during five months of immersion in deionized water; the small and random variations observed are included in the error deviation of the experimental balance. Thus, the result is

consistent with those conducted in SBF. However, ICP analyses after five months of immersion allow the determination of some differences between the different compositions. As a control, the water solution without scaffold exhibits a total absence of Calcium and Phosphate components. The water solutions with HA and 20HA/80β-TCP scaffolds show slight dissolutions of the CaP scaffolds. Finally, the ICP results show a much higher dissolution of Ca and P for the 60HA/40β-TCP scaffolds; ~20 times higher than HA which corresponds approximately to values reported in literature for such HA/β-TCP material [39,40]. To conclude, there is no noticeable weight loss in scaffold after immersion in SBF and water after one and five months, respectively. The ICP and weight loss measurement correspond well, which is an indication of the accurate measurement of the weight loss. The measurement of Ca and P ions in water indicates a faster degradation of BCP scaffolds than HA, especially for the 60HA/40β-TCP composition. A longer immersion time or a vigorous immersion condition is required to see a noticeable degradation of the scaffolds. *In vivo* studies may also provide more information on the performances of these scaffolds for the treatment of medium to high load-bearing bone defects.

4- Conclusion

HA/β-TCP composite scaffolds with structured porosity and controlled chemistry have been successfully fabricated by robocasting using water-based Pluronic inks. Three compositions, pure HA, 60HA/40β-TCP and 20HA/80β-TCP have been studied regarding their porosity, mechanical strength and biodegradation, which are key factors in determining scaffold performance. Scaffolds with mechanical strength ranging from ~3 to ~50 MPa were produced with a total porosity varying from ~80 to ~25 vol%, respectively. Variations in properties between the compositions were associated with the higher micro-porosity of composite scaffolds resulting from differences in the ink chemistries and in the sintering step. The fact that the macro-pore sizes being about hundred of micrometers and the compressive strengths equal to or higher than the range of human cancellous bone (2 – 12 MPa), indicates that the materials should permit bone ingrowth into the designed scaffolds for load-bearing bone substitute applications. For a given size of macro-pores, mechanical properties vary as a function of the composition in the following order HA > 20HA/80β-TCP > 60HA/40β-TCP. Besides, robocast scaffolds printed with various rod sizes, at a given porosity, show that stronger scaffolds were obtained from thin printed rods. This result suggests the scientific interest to fabricate thin structures for biomedical and various applications. No noticeable degradation of the scaffolds in SBF or water was observed, although there was a slight increase of Ca and P ions in water after 5 month. The work

reported here permits to classify the scaffolds regarding their different characteristics. Thus, this work should be a useful database in the choice of scaffold for tissue engineering applications. Ongoing *in vivo* studies in our research group may provide further guidance on the selection of scaffolds with the largest quantity of bone ingrowth.

Acknowlegments

This work was supported by the National Institutes of Health/National Institute of Dental and Craniofacial Research Grant No. 1 R01 DE015633. We acknowledge the support of the dedicated Xray tomography beamline 8.3.2 at the Advanced Light Source, funded by Department of Energy under contract no. DE-AC02-05CH11231. Russell Anderson from the Research Analytical Laboratory at the University of Minnesota (http://ral.cfans.umn.edu) is gratefully acknowledged for the ICP measurements.

References

[1] Hench LL. Bioceramics. J Am Ceram Soc 1998;81:1705.

[2] Hassna R.R. Ramay, Zhang M. Biphasic calcium phosphate nanocomposite porous scaffolds for load-bearing bone tissue engineering. Biomaterials 2004;25:5171.

[3] LeGeros RZ, Lin S, Rohanizadeh R, Mijares D, LeGeros JP. Biphasic calcium phosphate bioceramics: Preparation, properties and applications. Journal of Material Sciences in Medicine 2003;14:201.

[4] Daculsi G, LeGeros RZ, Nery E, Lynch K, Kerebel B. Transformation of biphasic calcium phosphate ceramics in vivo: Ultrastructural and physicochemical characterization. Journal of Biomedical Materials Research 1989;23(8):883.

[5] LeGeros RZ, Daculsi G, LeGeros JP. Bioactive Bioceramics. In: Orthopedic Biology and Medicine: Musculoskeletal Tissue Regeneration: Biological Materials and Methods, Chapter 8. Pietrzak WS, Editor. Humana Press Inc. New Jersey; 2008. p 153-181.

[6] LeGeros RZ, LeGeros JP, Hydroxyapatite, in Bioceramics and their Clinical Applications, Kokubo T, Editor., Woodhead Publishing Ltd. Cambridge; 2008. p. 367-394.

[7] Malard O, Guicheux J, Bouler JM, Gauthier O, Beauvillain de Montreuil C, Aguado E, Pilet P, LeGeros RZ, Daculsi G. Calcium phosphate scaffold and bone marrow for bone reconstruction in irradiated area: a dog study. Bone 2005;36:323.

[8] Arinzeh TL, Peter SJ, Archambault MP, Van Den Bos C, Gordon S, Kraus K, Smith A, Kadiyala S. Allogeneic mesynchymal stem cells rgenerate bone in a critical sized canine segmental defect. J Bone Joint Surgery American 2003;85A:1927.

[9] Miranda P, Pajares A, Saiz E, Tomsia AP, Guiberteau F. Mechanical properties of calcium phosphate scaffolds fabricated by robocasting. J Biomed Mater Res A 2008; 85A:218.

[10] De Groot K. Ceramics of calcium phosphates: preparation and properties. In: De Groot K, editor. Bioceramics of calcium phosphates. CRC Press, Boca Raton; 1983. p. 99-114.

[11] Nancollas GH. In vitro studies of calcium phosphate crystallisation. In: Mann S, Webb J, Williams RJP, editors. Biomineralization. Chemical and biochemical perspectives. VCH Publishers. Weinheim, Germany; 1989. p. 157-189.

[12] Daculsi G, Passuti N, Martin S, Deudon C, Legeros RZ, Raher S. Macroporous calcium phosphate ceramic for long bone surgery in humans and dogs: Clinical and histological study. Journal of Biomedical Materials Research 1990;24(3):379.

[13] Hulbert SF, Morrison SJ, Klawitte JJ. Tissue reaction to three ceramics of porous and non-porous structures. J Biomed Mater Res 1972;6:347.

[14] Langer R, Vacanti JP. Tissue engineering. Science 1993;260:920.

[15] Saiz E, Gremillard L, Menendez G, Miranda P, Gryn K, Tomsia AP. Preparation of porous hydroxyapatite scaffolds. Mat Sci Eng C Bio S 2007;27:546.

[16] Ben-Nissan B. Natural bioceramics: from coral to bone and beyond. Curr Opin Solid State Mater Sci 2003;7:283.

[17] Bohner M, Van Lenthe GH, Grunenfelder S, Hirsiger W, Evison R, Muller R. Synthesis and characterization of porous beta-tricalcium phosphate blocks. Biomaterials 2005;26:6099.

[18] Sous M, Bareille R, Rouais F, Clement D, Amedee J, Dupuy B, Baquey Ch. Cellular biocompatibility and resistance to compression of macroporous beta-tricalcium phosphate ceramics. Biomaterials 1998;19:2147.

[19] Deville S, Saiz E, Tomsia AP. Freeze casting of hydroxyapatite scaffolds for bone tissue engineering. Biomaterials 2006;27:5480.

[20] Franco J, Hunger P, Launey ME, Tomsia AP, Saiz E. Direct write assembly of calcium phosphate scaffolds using a water-based hydrogel. Acta Biomaterialia 2010;6:218.

[21] Miranda P, Saiz E, Gryn K, Tomsia AP. Sintering and robocasting of β-tricalcium phosphate scaffolds for orthopaedic applications. Acta Biomaterialia 2006;2:457.

[22] Miranda P, Pajares A, Saiz E, Tomsia AP, Guiberteau F, Fracture modes under uniaxial compression in hydroxyapatite scaffolds fabricated by robocasting. Journal of Biomedical Materials Research Part A 2007;83A:646.

[23] Duoss EB, Twardowski M, Lewis JA. Sol–gel inks for direct-write assembly of functional oxides. Adv Mater 2007;19:3485.

[24] Case ED, Smith IO, Baumann MJ. Microcracking and porosity in calcium phosphates and the implications for bone tissue engineering. Mat Sci Eng A Struct 2005;390:246.

[25] Kokubo T, Takadamaa H. How useful is SBF in predicting in vivo bone bioactivity?. Biomaterials 2006;27:2907.

[26] Murphy CM, Haugh MG, O'Brien FJ. The effect of mean pore size on cell attachment, proliferation and migration in collagen–glycosaminoglycan scaffolds for bone tissue engineering. Biomaterials 2010;31:461.

[27] Oh SH, Park IK, Kim JM, Lee JH. In vitro and in vivo characteristics of PCL scaffolds with pore size gradient fabricated by a centrifugation method. Biomaterials 2007;28:1664.

[28] Karageorgiou V, Kaplan D. Porosity of 3D biomaterial scaffolds and osteogenesis. Biomaterials 2005;26:5474.

[29] Petite H, Viateau V, Bensaïd W, Meunier A, De Pollak C, Bourguignon M, Oudina K, Sedel L, Guillemin G. Tissue-engineered bone regeneration. Nature Biotechnology 2000;18:959.

[30] Pineda LM, Büsing M, Meinig RP, Gogolewski S. Bone regeneration with resorbable polymeric membranes. III. Effect of poly(L-lactide) membrane pore size on the bone healing process in large defects. Journal of Biomedical Materials Research 1996;31:385.

[31] Wagoner Johnson AJ, Herschler BA. A review of the mechanical behavior of CaP and CaP/polymer composites for applications in bone replacement and repair. Acta Biomaterialia 2011;7:16.

[32] Cordell JM, Vogl ML, Wagoner Johnson AJ, The influence of micropore size on the mechanical properties of bulk hydroxyapatite and hydroxyapatite scaffolds, J Mech Behav Biomed Mater 2009;2:560.

[33] Bignon A, Chouteau J, Chevalier J, Fantozzi G, Carret J, Chavassieux P, Boivin G, Melin M, Hartmann D. Effect of micro- and macroporosity of bone substitutes on their mechanical properties and cellular response. J Mater Sci Mater Med 2003;14:1089.

[34] Genet M, Houmard M, Eslava S, Saiz E, Tomsia AP. A two-scale model of the mechanical behavior of ceramic scaffolds made by robocasting: possibilities and limits. (submitted to Acta Materialia)

[35] Raynaud S, Champion E, Bernache-Assollant D, Tetard D. Dynamic fatigue and degradation in solution of hydroxyapatite ceramics. Journal of Materials Science: Materials in Medicine 1998;9:221.

[36] Kwon SH, Jun YK, Hong SH, Kim HE. Synthesis and dissolution behavior of β-TCP and HA/β-TCP composite powders. Journal of the European Ceramic Society 2003;23:1039.

[37] Sanchez-Salcedo S, Balas F, Izquierdo-Barba I, Vallet-Regi M. In vitro structural changes in porous HA/β-TCP scaffolds in simulated body fluid. Acta Biomaterialia 2009;5:2738.

[38] Lu J, Descamps M, Dejou J, Koubi G, Hardouin P, Lemaitre J, Proust JP. The biodegradation mechanism of calcium phosphate biomaterials in bone. Journal of Biomedical Materials Research 2002;63:408.

[39] Kohri M, Miki K, Waite DE, Nakajima H, Okabe T. *In vitro* stability of biphasic calcium phosphate ceramics. Biomaterials 1993;14:299.

[40] Piattelli A, Scarano A, Mangano C.

Clinical and histologic aspects of biphasic calcium phosphate ceramic (BCP) used in connection with implant placement. Biomaterials 1996;17:1767.

Table and figure captions

Table 1: Average particle size and surface area of the HA, 60HA/40β-TCP and 20HA/80β-TCP as-received powders from Transtech. Note: HA powder contains 6.8 % of α-TCP.

Table 2: Composition of the inks used to print the robocast scaffolds.

Table 3: Amounts of calcium and phosphate ions (in mMol/L) introduced in the prepared SBF solution according to Kokubo [25] and amounts measured by ICP in the different SBF and water solutions into which the HA, 60HA/40β-TCP and 20HA/80β-TCP scaffolds were immersed. Ions amount into the SBF and water solutions without immersion of samples have been also quantified by ICP as a control.

Figure 1**:** Visualization of the HA/β-TCP robocast scaffolds after the sintering treatment. (A) Optical view of 20HA/80β-TCP scaffolds with two different pore sizes: 330 μm (left) and 150 μm (right) (pore size before sintering). (B), (C) and (D) are respectively corner, top and cross section views obtained by SEM of a HA scaffold with 330 μm pore size before sintering. (E) and (F) are the cross section micrographs of 60HA/40β-TCP and 20HA/80β-TCP scaffolds with pore of 330 μm and 620 μm before sintering, respectively. (G) and (H) illustrate 3-D visualizations of a 60HA/40β-TCP scaffold and one of its rod intersections, respectively, using synchrotron X-ray micro-computed tomography.

Figure 2: XRD spectra of robocast scaffolds after sintering at 1100°C with different HA/β-TCP compositions: (a) 100/0, (b) 60/40 and (c) 20/80. HA (⋆), β-TCP (o) and α-TCP (+) peaks are identified according to the JCPDS patterns 09-0432, 09-0169 and 09-0348, respectively. The spectrum of a 20HA/80β-TCP scaffolds sintered at 1140°C (d) is also drawn.

Figure 3: Shrinkage of the pure HA (a), 60HA/40β-TCP (b) and 20HA/80β-TCP (c) scaffolds after sintering in the three directions, x (//), y (\\) and z (■), as a function of the macro-pore size before sintering for scaffolds printed with a tip diameter of 250 μm.

Figure 4: Open (//) and total (■) volume porosity of the pure HA (a), 60HA/40β-TCP (b) and 20HA/80β-TCP (c) scaffolds after sintering as a function of the macro-pore size before sintering for scaffolds printed with a tip diameter of 250 μm.

Figure 5: Surface (top) and fracture (bottom) SEM micrographs of HA (A,D), 60HA/40β-TCP (B,E), and 20HA/80β-TCP (C,F) rods after sintering.

Figure 6: Compressive strength as a function of the robocast tip diameter for pure HA scaffolds with a constant volume porosity of 45 vol% ± 2.2. The insets represent characteristic strength x deformation curves of scaffolds fabricated with tip diameters of 250 μm (inset A) and 510 μm (inset B). The stars included in the inset illustrate some obvious cracks occurring in the structure during the compressive test.

Figure 7: Compressive strength along the z-axis as a function of the total porosity for the pure HA (o), 60HA/40β-TCP (□) and 20HA/80β-TCP (Δ) robocast scaffolds printed with different rod width and with a tip diameter of 250 μm. The inset compares the compressive tests performed along the z-axis (□) and perpendicularly to the z-axis (■) directions for the 60HA/40β-TCP scaffolds.

Figure 8: Compressive strength along the z-axis as a function of the macro-pore size before sintering for the pure HA (o), 60HA/40β-TCP (□) and 20HA/80β-TCP (Δ) robocast scaffolds printed with a tip diameter of 250 μm.

Figure 9: SEM micrographs of scaffolds printed with different design. Cross section (A) and top (B) views of a scaffold printed with a gradient porosity along the x and y axis. (C) Top view of a scaffold patterned with a radial gradient porosity (bone-like structure). (D) Cross section of a scaffold designed with an alternate structure. (E) Top view of a scaffold built with a gradient porosity along the z axis.

Figure 10: pH of the solution as a function of the immersion time in the SBF solution for HA (o), 60HA/40β-TCP (□) and 20HA/80β-TCP (Δ) robocast scaffolds.

Figure 11: Scaffold weight loss as a function of the immersion time in the SBF solution for the HA (o), 60HA/40β-TCP (□) and 20HA/80β-TCP (Δ) compositions.

Figure 12: Scaffold weight loss as a function of the immersion time in water for the HA (o), 60HA/40β-TCP (□) and 20HA/80β-TCP (Δ) compositions.

Table 1

	Average particle size (μm)	Surface area (m^2/g)	Comments
HA	1.999	4.0808	6.8 % of α-TCP
60HA/40β-TCP	2.057	3.503	
20HA/80β-TCP	2.082	3.2272	

Table 1: Average particle size and surface area of the HA, 60HA/40β-TCP and 20HA/80β-TCP as-received powders from Transtech. Note: HA powder contains 6.8 % of α-TCP.

Table 2

	HA	60HA/40β-TCP	20HA/80β-TCP
Ceramic (wt%)	74.1	66.6	61.2
DiWater (wt%)	20.7	26.7	31
F-127 (wt%)	5.2	6.7	7.8

Table 2: Composition of the inks used to print the robocast scaffolds.

Table 3

	SBF compo. [25]	ICP measurements (Deviation < 0.05 mMol/L)							
		Scaffolds in SBF (1 month)				Scaffolds in water (5 months)			
		Control	HA	60/40	20/80	Control	HA	60/40	20/80
Ca^{2+}	2.5	2.49	2.53	1.38	1.46	0.00	0.09	3.30	0.41
HPO_4^{2-}	1	1.04	1.04	0.10	0.06	0.01	0.31	6.00	0.34

Table 3: Amounts of calcium and phosphate ions (in mMol/L) introduced in the prepared SBF solution according to Kokubo [25] and amounts measured by ICP in the different SBF and water solutions into which the HA, 60HA/40β-TCP and 20HA/80β-TCP scaffolds were immersed. Ions amount into the SBF and water solutions without immersion of samples have been also quantified by ICP as a control.

Figure 1

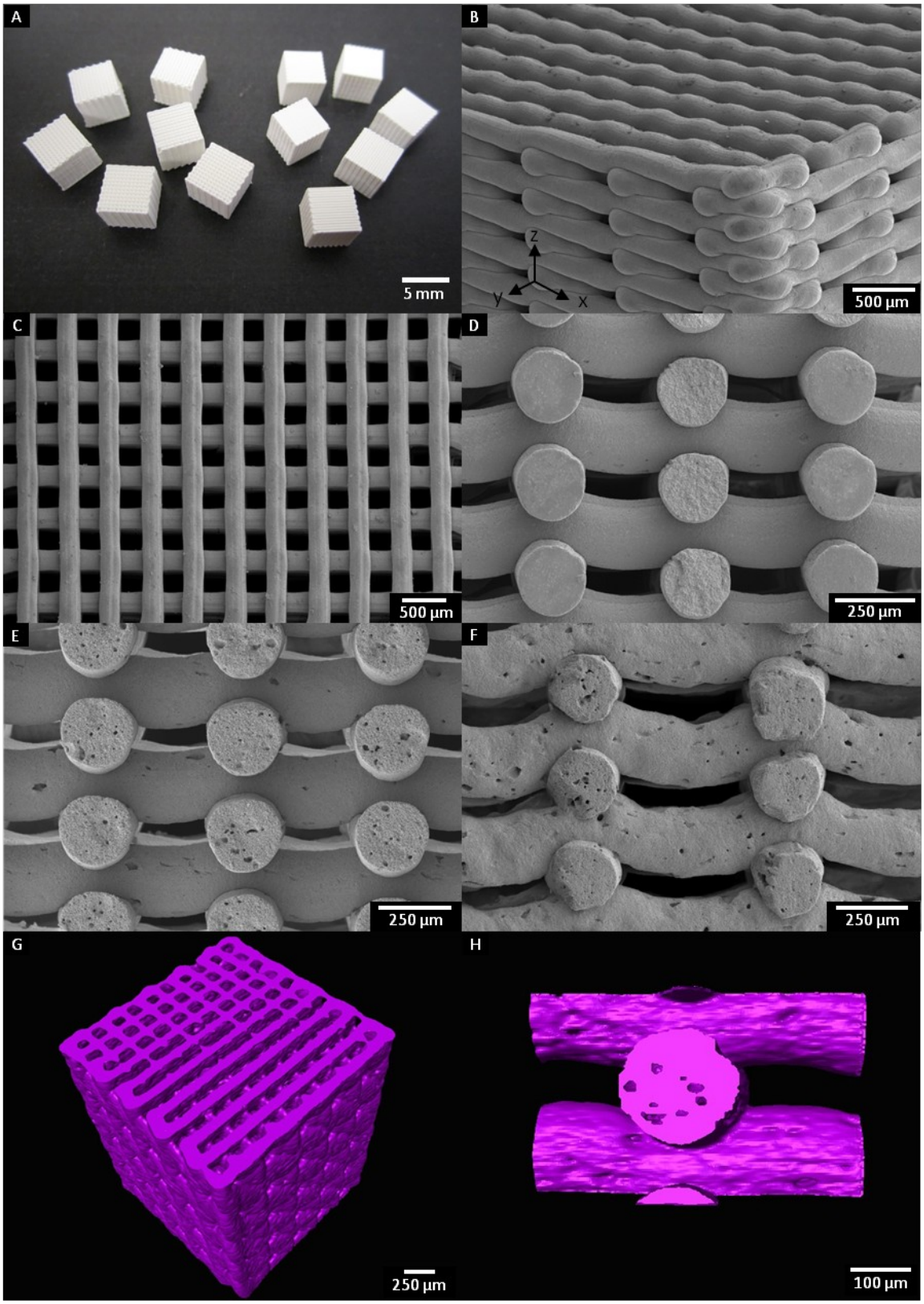

Figure 1**:** Visualization of the HA/β-TCP robocast scaffolds after the sintering treatment. (A) Optical view of 20HA/80β-TCP scaffolds with two different pore sizes: 330 µm (left) and 150 µm (right) (pore size before sintering). (B), (C) and (D) are respectively corner, top and cross section views obtained by SEM of a HA scaffold with 330 µm pore size before sintering. (E) and (F) are the cross section micrographs of 60HA/40β-TCP and 20HA/80β-TCP scaffolds with pore of 330 µm and 620 µm before sintering, respectively. (G) and

(H) illustrate 3-D visualizations of a 60HA/40β-TCP scaffold and one of its rod intersections, respectively, using synchrotron X-ray micro-computed tomography.

Figure 2

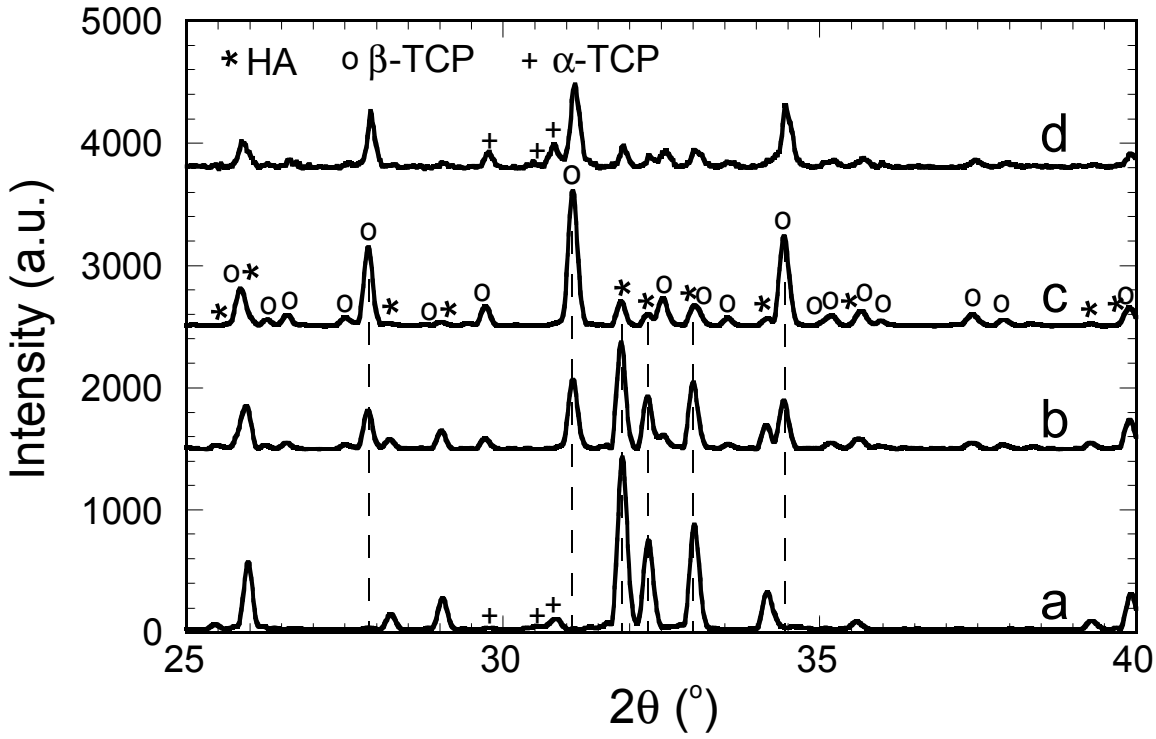

Figure 2: XRD spectra of robocast scaffolds after sintering at 1100°C with different HA/β-TCP compositions: (a) 100/0, (b) 60/40 and (c) 20/80. HA (⋆), β-TCP (o) and α-TCP (+) peaks are identified according to the JCPDS patterns 09-0432, 09-0169 and 09-0348, respectively. The spectrum of a 20HA/80β-TCP scaffolds sintered at 1140°C (d) is also drawn.

Figure 3

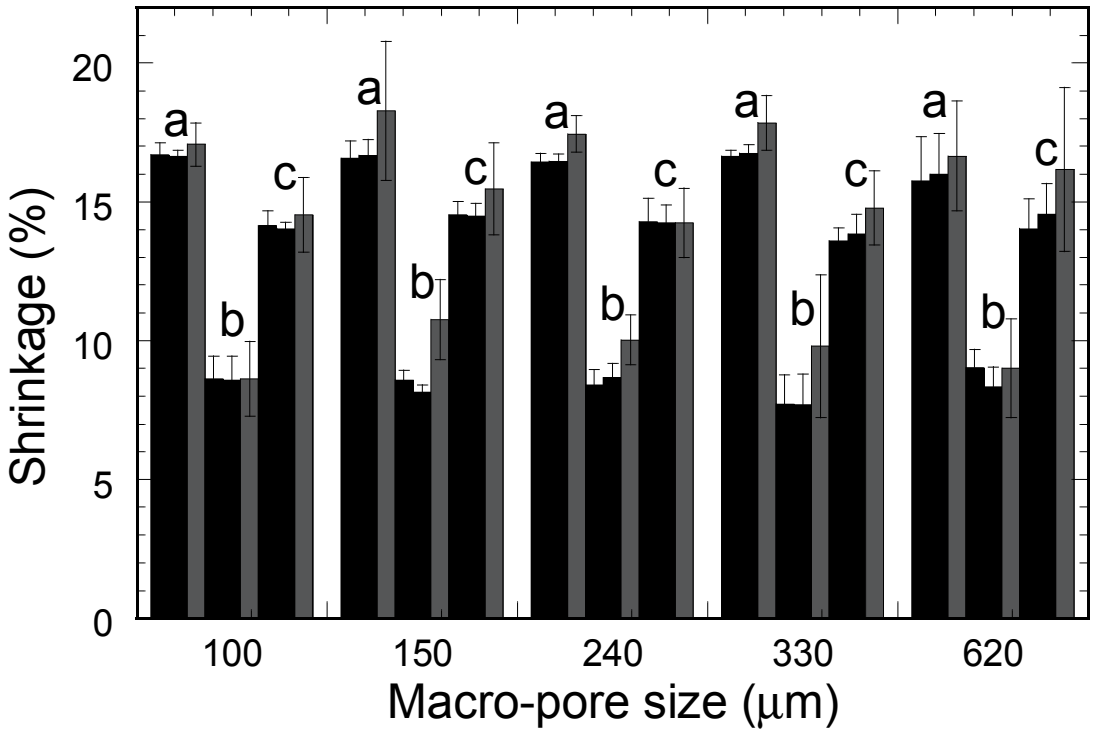

Figure 3: Shrinkage of the pure HA (a), 60HA/40β-TCP (b) and 20HA/80β-TCP (c) scaffolds after sintering in the three directions, x (//), y (\\) and z (■), as a function of the macro-pore size before sintering for scaffolds printed with a tip diameter of 250 μm.

Figure 4

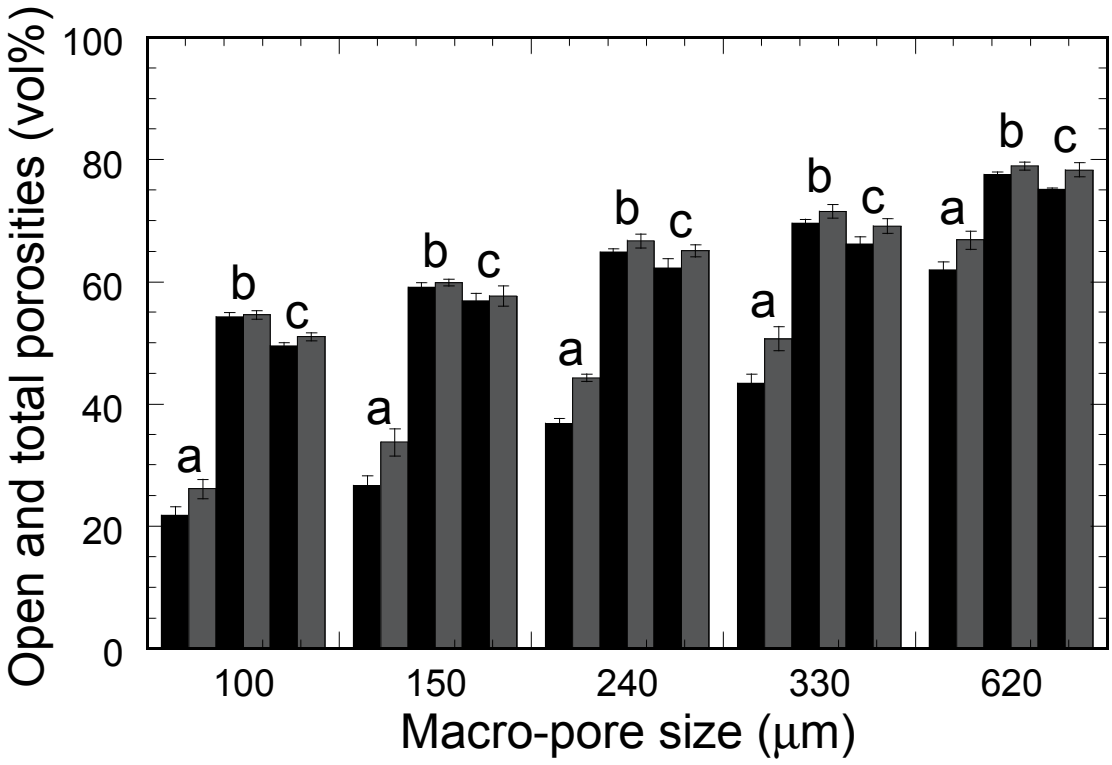

Figure 4: Open (//) and total (■) volume porosity of the pure HA (a), 60HA/40β-TCP (b) and 20HA/80β-TCP (c) scaffolds after sintering as a function of the macro-pore size before sintering for scaffolds printed with a tip diameter of 250 μm.

Figure 5

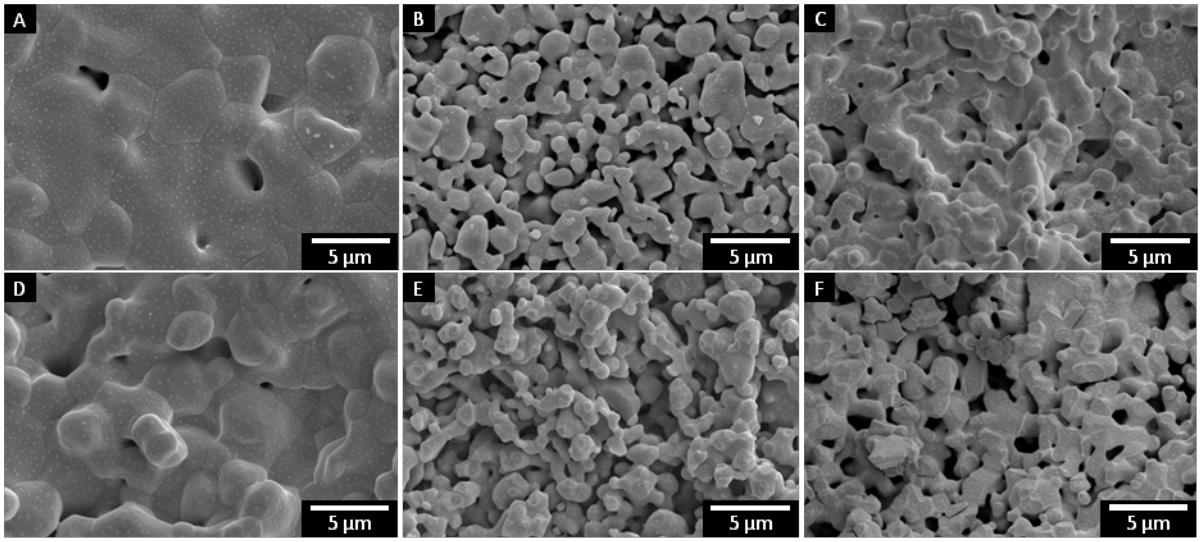

Figure 5: Surface (top) and fracture (bottom) SEM micrographs of HA (A,D), 60HA/40β-TCP (B,E), and 20HA/80β-TCP (C,F) rods after sintering.

Figure 6

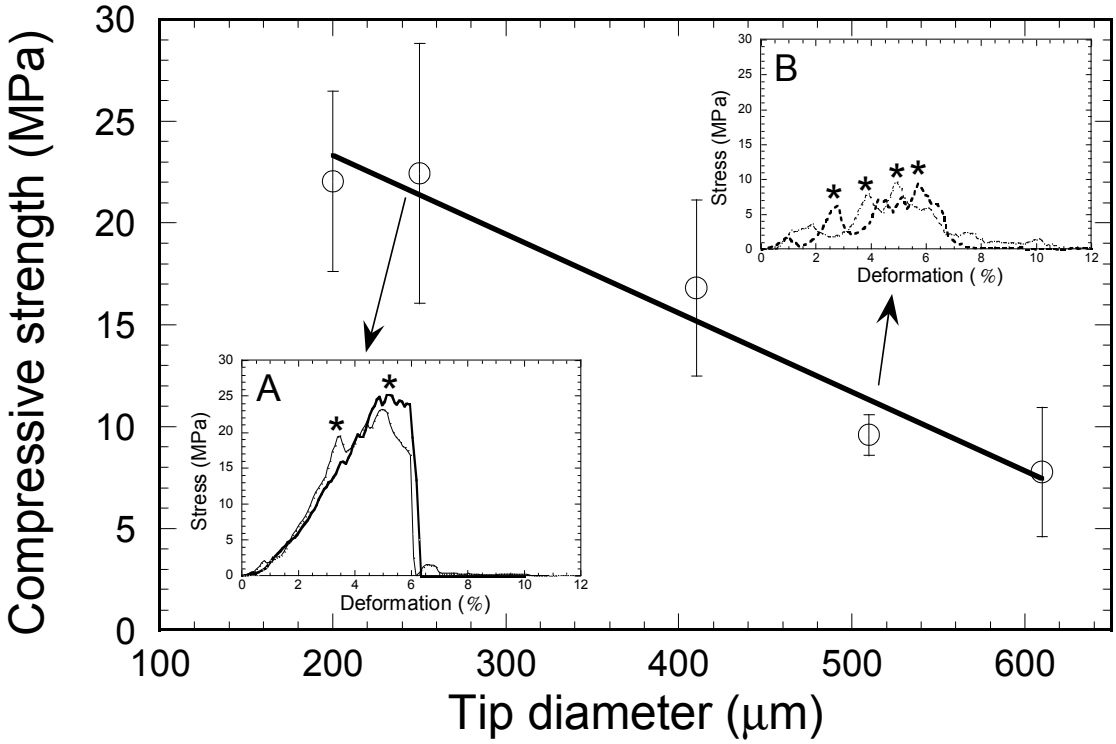

Figure 6: Compressive strength as a function of the robocast tip diameter for pure HA scaffolds with a constant volume porosity of 45 vol% ± 2.2. The insets represent characteristic strength x deformation curves of scaffolds fabricated with tip diameters of 250 μm (inset A) and 510 μm (inset B). The stars included in the inset illustrate some obvious cracks occurring in the structure during the compressive test.

Figure 7

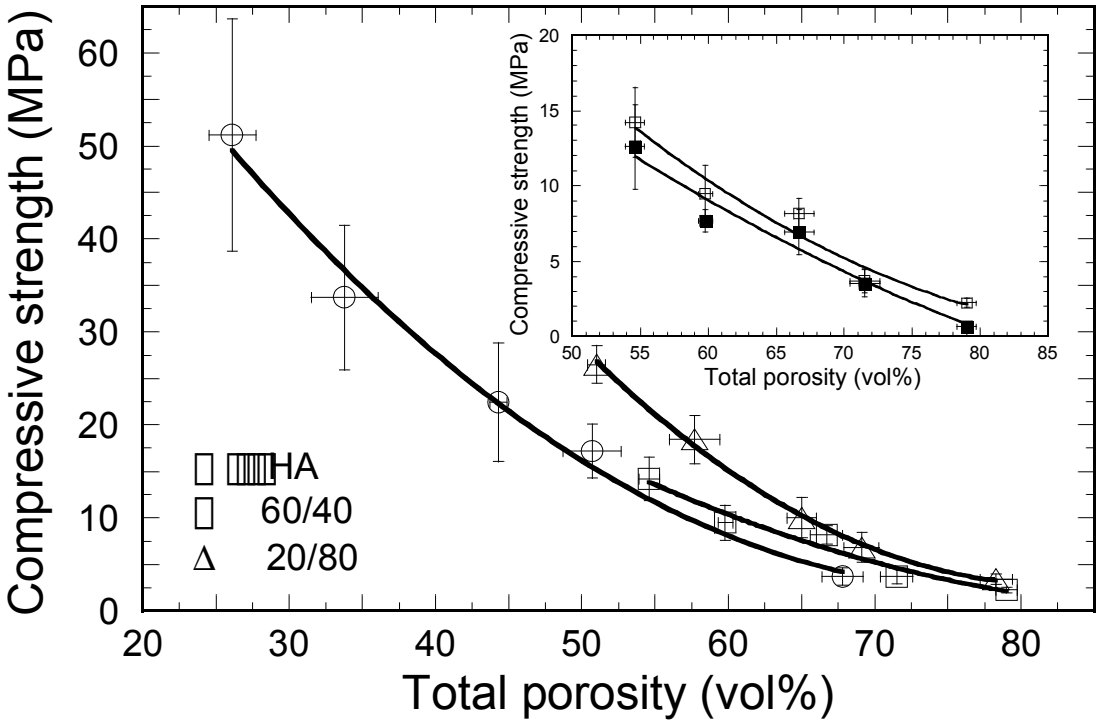

Figure 7: Compressive strength along the z-axis as a function of the total porosity for the pure HA (o), 60HA/40β-TCP (□) and 20HA/80β-TCP (Δ) robocast scaffolds printed with different rod width and with a tip diameter of 250 μm. The inset compares the compressive tests performed along the z-axis (□) and perpendicularly to the z-axis (■) directions for the 60HA/40β-TCP scaffolds.

Figure 8

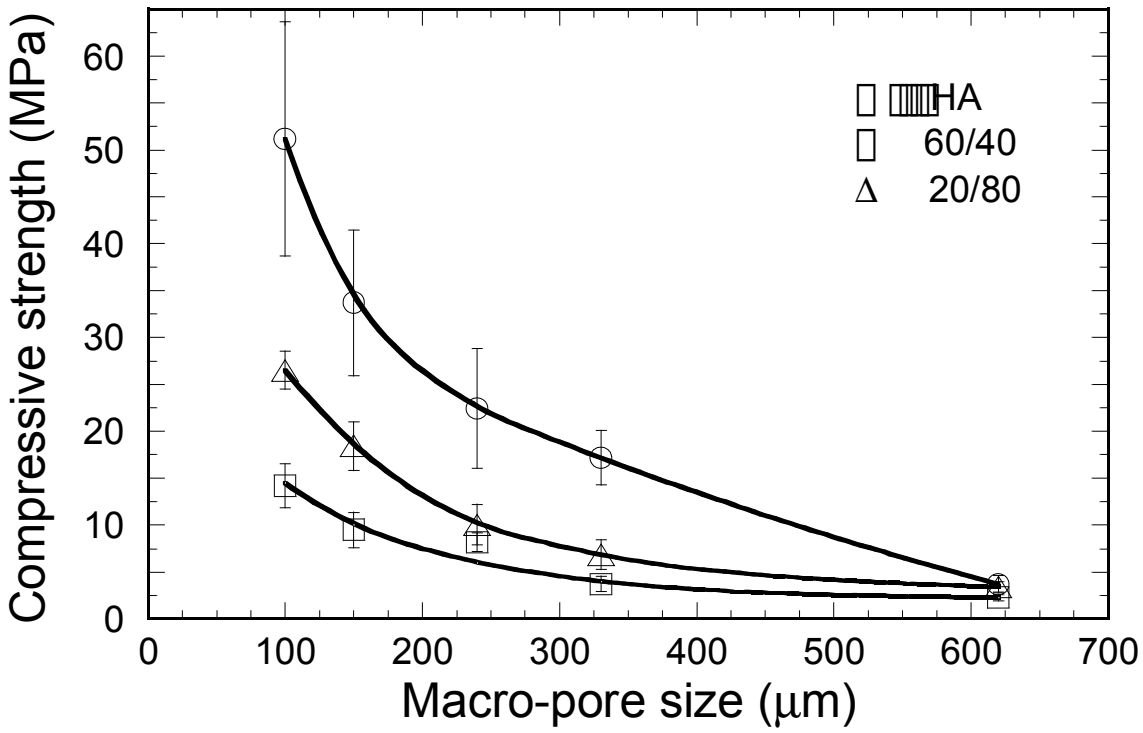

Figure 8: Compressive strength along the z-axis as a function of the macro-pore size before sintering for the pure HA (o), 60HA/40β-TCP (□) and 20HA/80β-TCP (Δ) robocast scaffolds printed with a tip diameter of 250 μm.

Figure 9

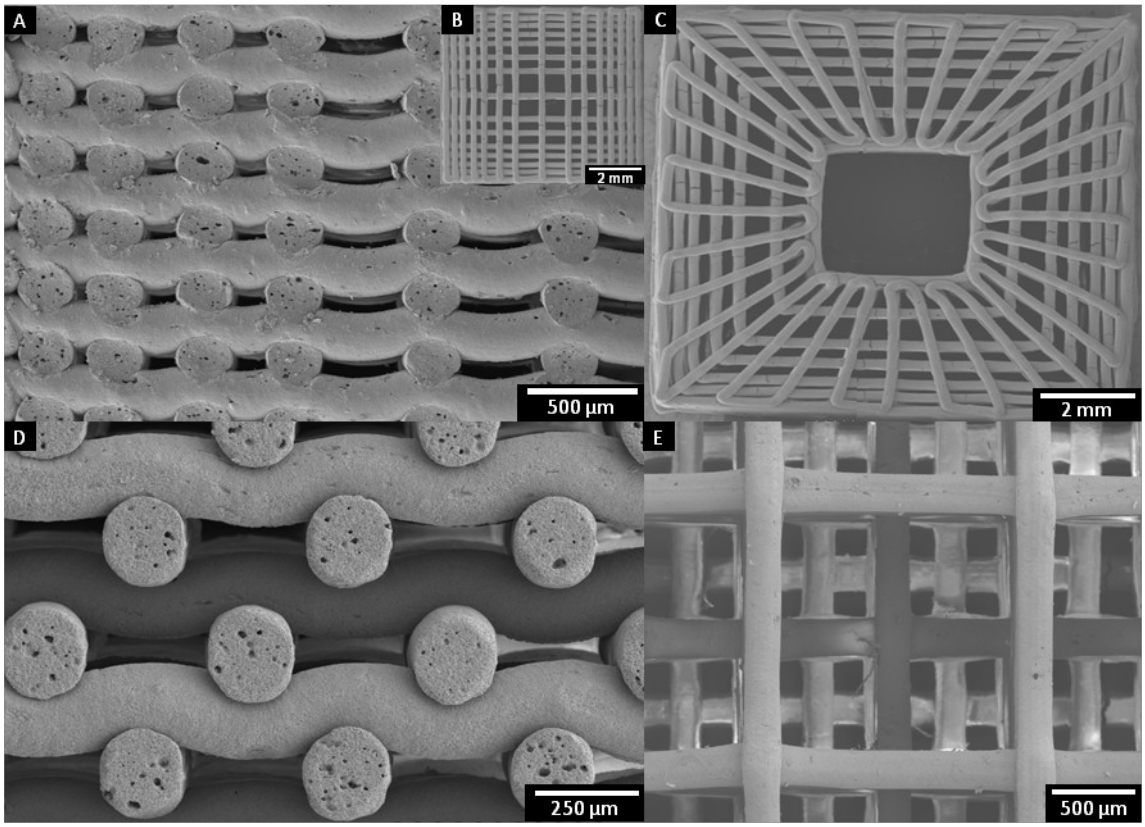

Figure 9: SEM micrographs of scaffolds printed with different design. Cross section (A) and top (B) views of a scaffold printed with a gradient porosity along the x and y axis. (C) Top view of a scaffold patterned with a radial gradient porosity (bone-like structure). (D) Cross section of a scaffold designed with an alternate structure. (E) Top view of a scaffold built with a gradient porosity along the z axis.

Figure 10

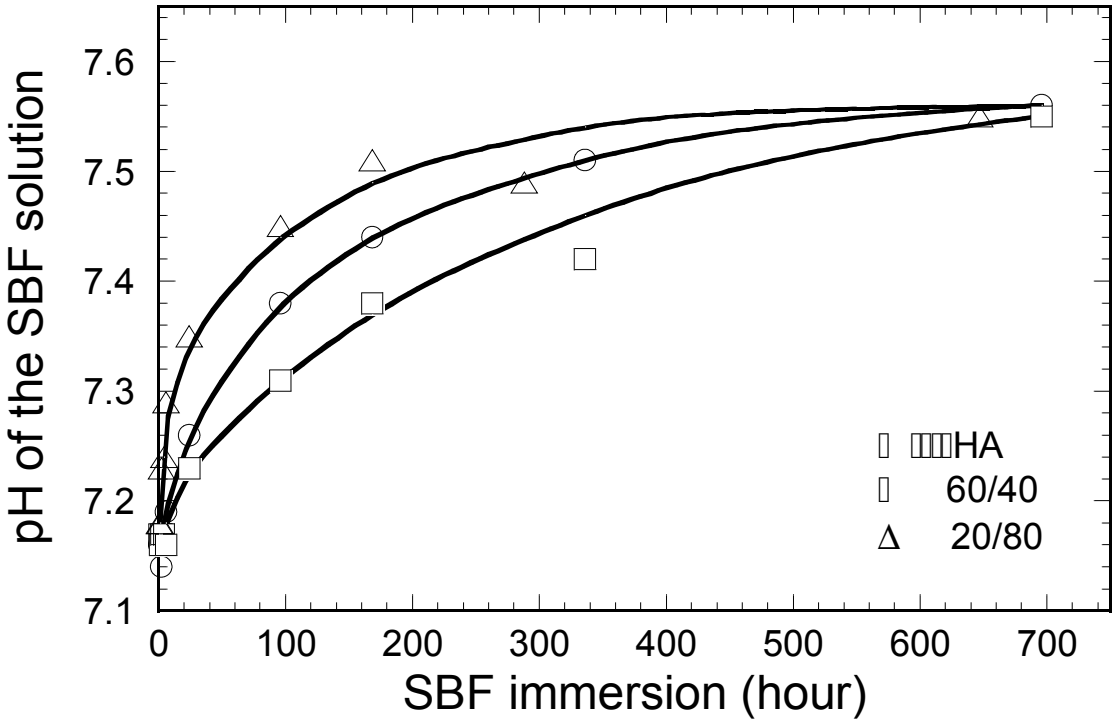

Figure 10: pH of the solution as a function of the immersion time in the SBF solution for HA (o), 60HA/40β-TCP (□) and 20HA/80β-TCP (Δ) robocast scaffolds.

Figure 11

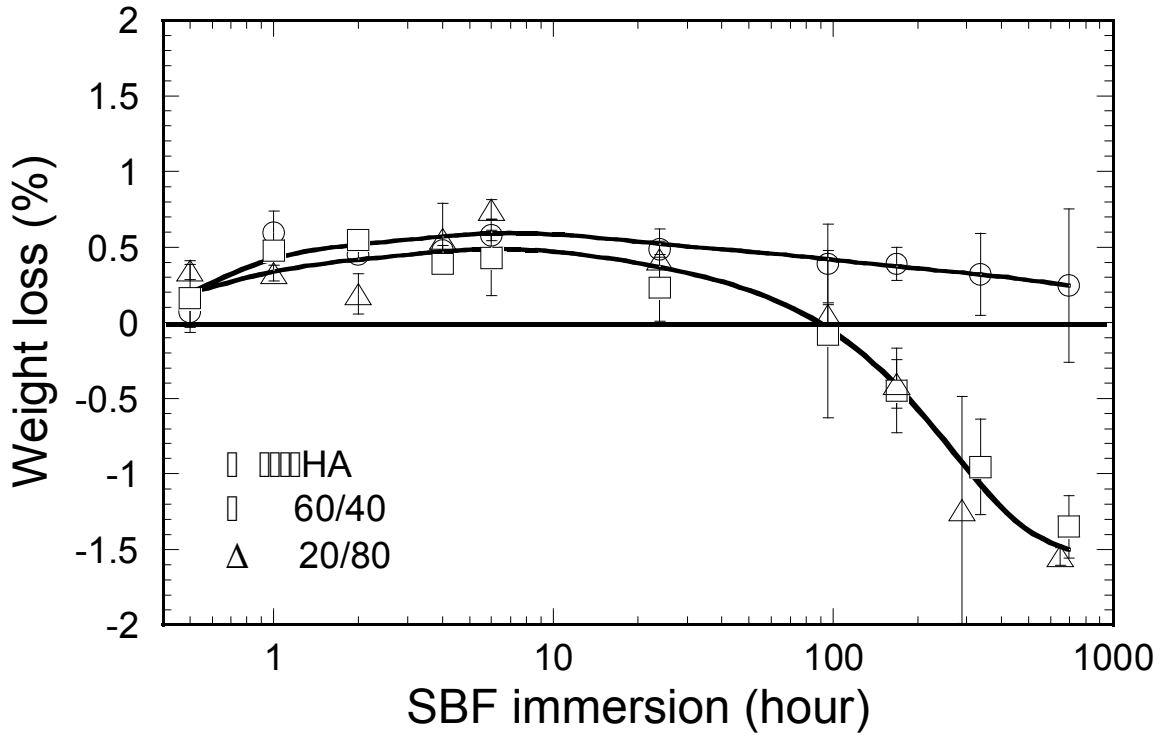

Figure 11: Scaffold weight loss as a function of the immersion time in the SBF solution for the HA (o), 60HA/40β-TCP (□) and 20HA/80β-TCP (∆) compositions.

Figure 12

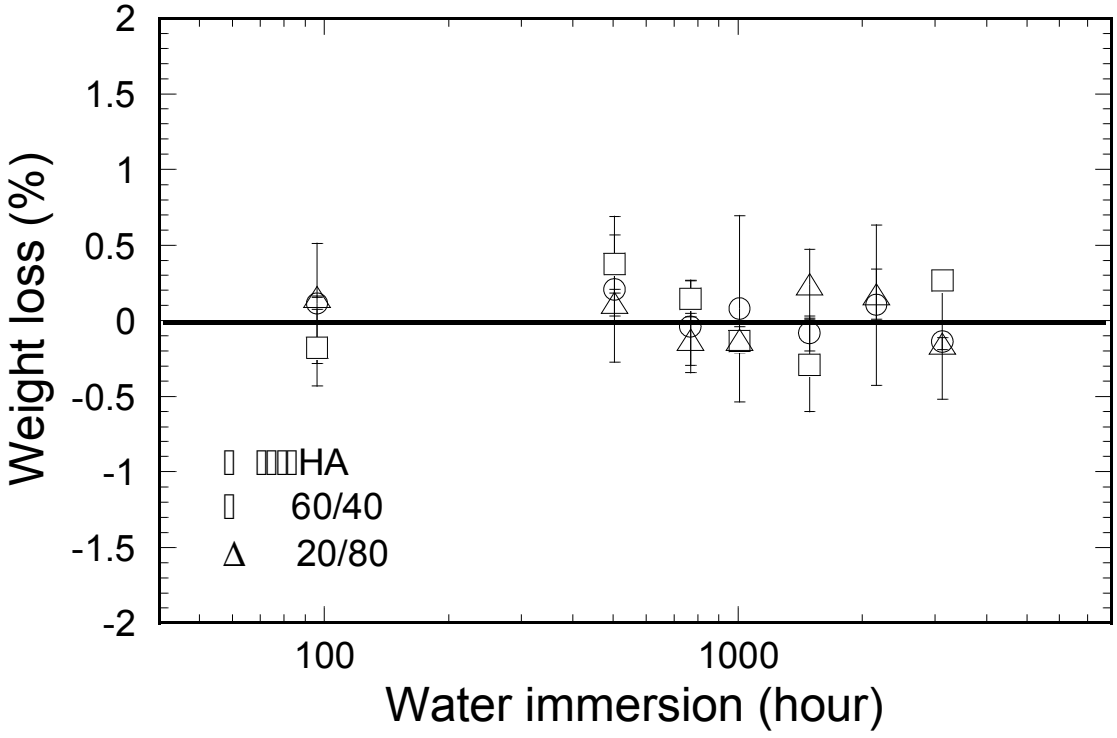

Figure 12: Scaffold weight loss as a function of the immersion time in water for the HA (o), 60HA/40β-TCP (□) and 20HA/80β-TCP (Δ) compositions.